Image-model coupling: application to an ionospheric storm

N.D. Smith[1,*], *D. Pokhotelov*[2], *C.N. Mitchell*[2], *C.J. Budd*[1]

[1] *Department of Mathematical Sciences, University of Bath, U.K., BA2 7AY*
[2] *Department of Electronic and Electrical Engineering, University of Bath, U.K., BA2 7AY*
[*] *Completed while with the Department of Electronic and Electrical Engineering, University of Bath*

Bath Institute For Complex Systems

Preprint 17/08 (2008)

http://www.bath.ac.uk/math-sci/BICS

Image-model coupling: application to an ionospheric storm

N.D. Smith[1,*], D. Pokhotelov[2], C.N. Mitchell[2], C.J. Budd[1]

[1] Department of Mathematical Sciences, University of Bath, U.K., BA2 7AY

[2] Department of Electronic and Electrical Engineering, University of Bath, U.K., BA2 7AY

[*] Completed while with the Department of Electronic and Electrical Engineering, University of Bath

October 2008

(updated on October 12, 2008)

Abstract: Techniques such as tomographic reconstruction may be used to provide images of electron content in the ionosphere. Models are also available which attempt to describe the dominant physical processes operating in the ionosphere, or the statistical relationships between ionospheric variables. The process of coupling model output to images can be used to infer the values of driver variables which best replicate some description of electron content imaged in the ionosphere, according to some criterion such as a matching function. Coupling may also be used to explore the sensitivity of the electron content to variations in the values of those driver variables. By way of illustration, an ionospheric model is coupled to a tomographic reconstruction of the geomagnetic storm of 20 November 2003, for a region above north America. A simple model is chosen to reduce the number of input drivers that are varied. The investigation suggests better coupling can be obtained by increasing the ratio of O to N_2 neutral densities, and with relatively high $\boldsymbol{E} \times \boldsymbol{B}$ drift velocity at the geomagnetic equator. However the conclusions drawn are conditional on the accuracy of the assumptions in the ionospheric model and the accuracy of the tomographic reconstruction. As such, the search for the 'best' coupling between images and model output may often give extra insight into the limitations of the model being used.

1 Introduction

The ionosphere is a complex system with multiple processes operating at different scales. Understanding these processes is of scientific value, and has practical benefit in applications such as communication and navigation. In recent years, different empirical and physical models have been developed to explain how the ionosphere, typically in terms of its plasma content, responds to external stimuli or drivers. The mapping from the space of driver variables to the space of variables describing the ionosphere is expected to be nonlinear, especially for an extreme event such as a geomagnetic storm. Hence it is interesting to study the sensitivity of the response to different drivers. This may give further insight into which processes dominate under different conditions. Also, those drivers to which the response is most sensitive may require more accurate or more frequent measurement in future.

One means of investigating the ionosphere, including sensitivity of its response to drivers, is via image-model coupling. Images of electron density may be obtained, for example, by tomographic reconstruction techniques [2] [15]. Once a sequence of images is obtained for an ionospheric event, an ionospheric model is then selected, its drivers varied, and the closeness of match between the model output and image sequence calculated. The shape of the matching function gives an indication of sensitivity, for the particular event and subject to the accuracy of the ionospheric model. This approach also encourages a better appreciation of the limitations and assumptions in the ionospheric model being used. A framework for describing

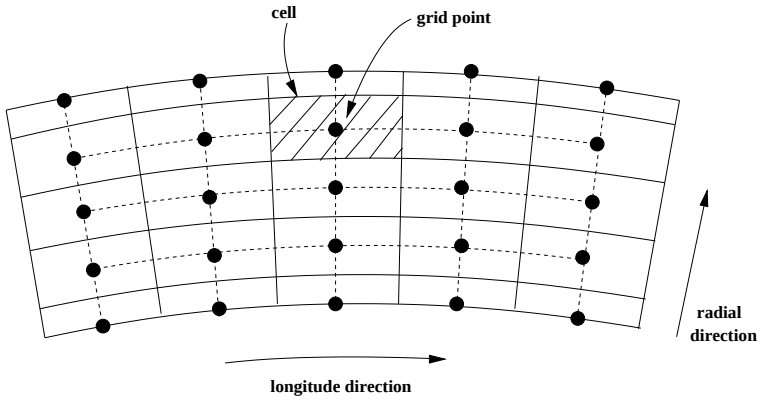

Figure 1: Sketch showing how grid points are related to cells.

image-model coupling in terms of communication along a discrete channel is presented in [18]. This paper describes a simple application of these ideas to an extreme event, the geomagnetic storm of 20 November 2003. For simplicity, much of the memory in the system is ignored in deriving the matching function, i.e. many of the statistical conditional dependencies between data at successive timesteps are ignored. The features and matching function are described briefly in Section 2. The tomographic reconstruction is presented in Section 3, and the analysis for an ionospheric model in Section 4. Some discussion and conclusions follow in Section 5 and Section 6 respectively.

2 Calculating features and optimising the match

It is often convenient to calculate ionospheric data at a discrete set of points on a grid which is uniform in altitude, and geographic latitude and longitude coordinates. The grid points are represented as blackened circles in the sketch of a slice of constant geographic latitude in Figure 1. Assume the grid is indexed by (l, m, n) where $l \in [1, L]$ is an index for altitude above the Earth's surface, $m \in [1, M]$ for geographic latitude and $n \in [1, N]$ for geographic longitude. The altitude of a grid point is $h_g(l, m, n)$ and the electron density at that point is $N_g(l, m, n)$. The grid points are used to define cells in the manner of Figure 1 where grid points are cell centres; the exceptions are the 'half-cells' at the top and foot of the cell structure. Hence cell centres are defined with the following altitudes. For all l, m,

$$h_c(l,m,n) \quad = \quad \begin{cases} \frac{3}{4}h_g(L,m,n) + \frac{1}{4}h_g(L-1,m,n) & \text{if} \quad l = L \\ h_g(l,m,n) & \text{if} \quad 1 < l < L \\ \frac{3}{4}h_g(1,m,n) + \frac{1}{4}h_g(2,m,n) & \text{if} \quad l = 1 \end{cases}, \tag{1}$$

where it is assumed $L > 1$. The electron densities at the cell centres are defined such that $N_c(l, m, n) = N_g(l, m, n)$, $\forall l, m, n$. Electron density is assumed uniform in a cell. The cells are contiguous, and each cell has a vertical length $d(l, m, n)$. The electron content of the ionosphere may be summarised using vertical total electron content (VTEC) or mean ionospheric height (i.e. the height of the centre of mass of the electrons). These may be respectively calculated as follows,

$$\text{VTEC}(m,n) \quad = \quad \sum_{l=1}^{L} d(l,m,n) N_c(l,m,n), \tag{2}$$

and,

$$\bar{h}(m,n) \quad = \quad \sum_{l=1}^{L} h_c(l,m,n) \frac{N_c(l,m,n) d(l,m,n)}{\sum_{a=1}^{L} N_c(a,m,n) d(a,m,n)}. \tag{3}$$

The 2-dimensional maps may then be assembled into a column vector, for example the $(MN \times 1)$ feature vector,

$$\boldsymbol{z} \quad = \quad (\mathrm{VTEC}(1,1), \ldots \mathrm{VTEC}(M,N))^{\top}. \tag{4}$$

Alternatively a $(MN \times 1)$ feature space may be defined on mean ionospheric heights alone, or a $(2MN \times 1)$ feature space defined on both VTECs and mean ionospheric heights. Given an image sequence $\tilde{\boldsymbol{z}}(1,T) = (\tilde{\boldsymbol{z}}(1), \ldots, \tilde{\boldsymbol{z}}(T))$ and model output $\boldsymbol{z}(1,T) = (\boldsymbol{z}(1), \ldots, \boldsymbol{z}(T))$, a matching function may be defined which measures the closeness of match between the two sequences [18],

$$f(\boldsymbol{z}(1,T), \tilde{\boldsymbol{z}}(1,T)) \quad = \quad \sum_{t=1}^{T} \boldsymbol{z}(t)^{\top} (\frac{1}{2}\boldsymbol{z}(t) - \tilde{\boldsymbol{z}}(t)). \tag{5}$$

Given competing model outputs, the output of closest match is,

$$\hat{\boldsymbol{z}}(1,T) \quad = \quad \underset{\boldsymbol{z}(1,T)}{\operatorname{argmin}} f(\boldsymbol{z}(1,T), \tilde{\boldsymbol{z}}(1,T)), \tag{6}$$

where a perfect match yields a nonpositive value for the matching function. In the following experiments, each output sequence is obtained by fixing a subset of driver variables at a value $\boldsymbol{u}$. Hence,

$$\hat{\boldsymbol{u}} \quad = \quad \underset{\boldsymbol{u}}{\operatorname{argmin}} f(\boldsymbol{u}, \tilde{\boldsymbol{z}}(1,T)), \tag{7}$$

where $\boldsymbol{u} \mapsto \boldsymbol{z}(1,T)$ is assumed injective. For convenience, the objective function is sometimes abbreviated to f. Also, when there are multiple time windows and each is treated separately, the notation f^s is used to describe the objective function for the sth time window. The minimisation above yields the least sum squares estimate. As described more fully in [18], this estimate may be regarded as the maximum a-posteriori estimate subject to a very simple discrete channel model (i.e. there is no channel memory, and channel noise is assumed Gaussian white noise which is stationary in time and spatially with respect to the value of $\boldsymbol{z}(t)$). The channel model is overly simple for such a complex system as the ionosphere, but permits the derivation of a matching function which is relatively easy to evaluate and which does not require estimates for statistical models.

3 Tomographic reconstruction using MIDAS

MIDAS ('Multi-Instrument Data Analysis System') version 2.0 [12] [19] was used to tomographically reconstruct electron densities in the northern hemisphere using the total electron content along raypaths between satellites and IGS receiver stations. The reconstruction was for 0100h UT to 2300h UT inclusive on 20 November 2003 at 10 minute intervals, and over a $(39 \times 17 \times 73)$ structure of grid points (this included altitudes at 90km, and from 100km to 1580km inclusive at 40km intervals; geographic latitudes from 0°N to 80°N inclusive at 5° intervals; geographic longitudes from 180°W to 180°E inclusive at 5° intervals). Data were collected from 58 IGS stations, about 20-or-so of which were located under or near the L-shaped region above north America used in the image-model coupling investigation. Otherwise, the parameterisation of MIDAS was similar or identical to that used in [19]. Vertical electron density profiles were approximated using two empirical orthogonal basis functions. The basis function coefficients defined the state space for the Kalman filter. The state vector was initialised using the International Reference Ionosphere, 1995 (IRI-95) [1]. State evolution was governed by a projection matrix describing Gaussian diffusion of plasma, with appropriate scaling using a model of electric potentials [22] (this 'Weimer model' required Interplanetary Magnetic Field (IMF) and solar wind data as input). Furthermore, for each step of the Kalman filter, the state prediction was linearly weighted with the IRI-95 model in a 19:1 ratio. Adhoc estimates were used for the noise covariances, and the covariance of the prior on the initial state estimate. There was also some data cleaning of total electron content values, using a threshold of four standard deviations.

The tomographic reconstruction for the northern hemisphere, up to 80°N, shows a localised increase in electron densities at 1200h/1300h UT, its appearance corresponding to the onset of the storm, as shown

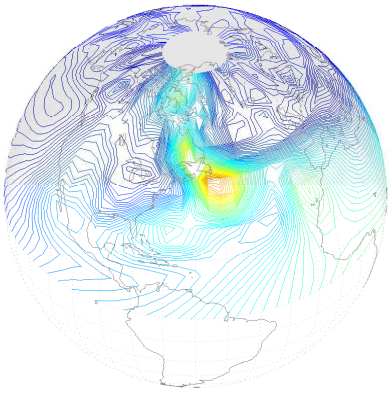

1600h UT

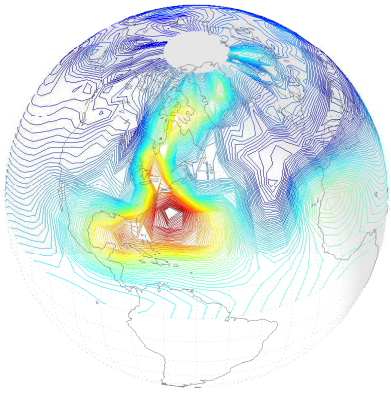

1800h UT

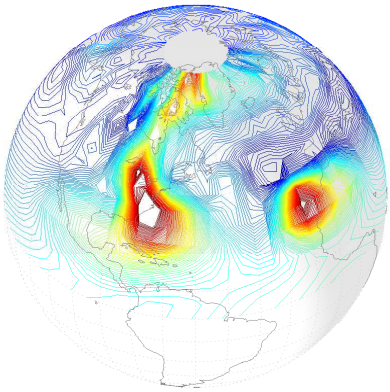

1900h UT

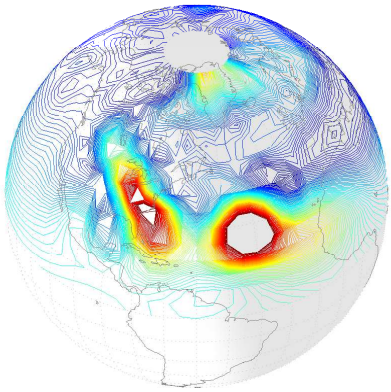

2100h UT

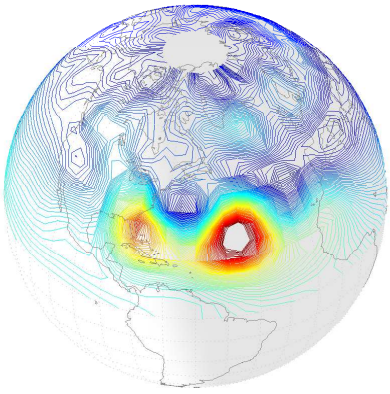

2200h UT

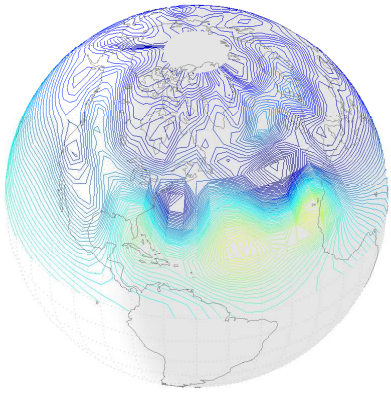

2300h UT

Figure 2: Contour plots for vertical total electron content by MIDAS during 20 November 2003 (contours from 0 to 100 TEC units at 1 unit intervals, where 1 TEC unit $= 1 \times 10^{16}$ electrons/m^2).

by a southward turning of the IMF (see Figure 6). The localised intensification of plasma rotates with the sun till about 1800h UT, then corotates with the Earth. Between 1600h and 2000h UT, but particularly at 1900h UT, there is evidence of a high-latitude intensification, or so-called ionisation tongue, near local noon. The reconstruction is unreliable above the Atlantic due to the very sparse coverage of receivers there. However, as described later, only part of the image above north America is used in the image-model coupling investigation. Nevertheless, it is useful to understand what ionospheric processes may be occurring on a larger scale.

As the IMF turns southward, promptly penetrating electric fields [11] [21] are thought to penetrate into the inner plasmasphere and ionosphere in an eastward direction, enhancing the equatorial fountain and lifting plasma upwards and across to more northerly midlatitude locations. However the ionisation tongue is thought to be caused by strong high-latitude convection, for example the so-called subauroral polarisation stream [6]. The reconstruction therefore suggests the presence, and hence interaction, of both equatorial/low latitude and subauroral/ high latitude processes. In addition, electron precipitation and Joule heating are likely during geomagnetic storms, causing strong equatorward thermospheric winds [11]. Neutral winds and electric fields can lift plasma upwards along field lines, thereby providing mechanisms to increase vertical total electronp content at high and midlatitude locations.

4 Coupling with SAMI2

SAMI2 ('Sami2 is Another Model of the Ionosphere') version 0.98 [16] [8] is a physics-based model of the ionosphere which solves 'first principles equations' describing ionospheric plasma. SAMI2 is able to model plasma along field lines, but constrained within a slice of constant geomagnetic longitude, i.e. a flux tube. Here, there were 10 different field lines within a slice where the maximum altitudes of the highest and lowest field lines were fixed at 10,000.0km and 100.0km respectively, and the base of field lines was fixed at 90.0km. Densities were calculated at 101 points spaced along each field line. In total, eight different slices were chosen, where the slices were anchored to intersection points defined at 100.0km altitude, 40°N geographic latitude, and geographic longitude from 60.0 °W to 130.0 °W inclusive at 10° intervals. Seven ion species were modelled by SAMI2. Quasineutrality was assumed in this analysis and the sum of the seven ion densities at a point was taken as the local electron density at that point. The optimisation of SAMI2 against MIDAS was restricted to a L-shaped region above north America where the reconstruction was expected to be more reliable. In geographic coordinates, the region included grid points from 20°N to 40°N inclusive in 5° intervals, 70°W to 120°W inclusive in 10° intervals, with the exception of $(20°\text{N}, 120°\text{W})$ and $(25°\text{N}, 120°\text{W})$; grid points were at altitudes from 100km to 1580km inclusive in intervals of 40km, and also at 90km (for example, see Figure 5 for visualisation). The nonuniformly-spaced set of electron density values from SAMI2 were then mapped to the L-shaped region by nearest pixel sampling, where any ties were resolved by precedence in scan order. In the following experiments, each SAMI2 run was started at 0000h UT and lasted 48 hours (during which SAMI2 does not update its 'day of year'). To reduce the effect of transients, hourly output was collected during the appropriate time window between 24 and 48 hours after the start of each run; hence for the earliest time window beginning at 1200h UT, SAMI2 was allowed to run for a full 36 hours before output was collected. Two of the principal driver variables for SAMI2 were $F_{10.7}$ and Ap which are respectively measures of solar and geomagnetic activity [7]. The 3-monthly average for $F_{10.7}$ was fixed to the current $F_{10.7}$ value. The parameter associated with photoelectron heating was fixed at $3.0 \times 10^{-14}\text{cm}^2$. The sinusoidal $\boldsymbol{E} \times \boldsymbol{B}$ drift velocity model was used [8], parameterised by V and described in Appendix A. The maximum number of timesteps was set to 20×10^6. All other values which were not directly varied in the following experiments were set to their recommended or default settings; in particular, multiplicative factors for neutral wind speed, $\boldsymbol{E} \times \boldsymbol{B}$ drift velocity, neutral densities corresponding to the 7 positive ion species, and neutral temperature were all kept at unity unless otherwise stated.

time window		VTEC			$\bar{h}$			VTEC and $\bar{h}$		
s	(UT)	$F_{10.7}$	Ap	V/ms^{-1}	$F_{10.7}$	Ap	V/ms^{-1}	$F_{10.7}$	Ap	V/ms^{-1}
1	1200h - 1400h	150.0	0	300.0	300.0	0	375.0	300.0	15	300.0
2	1500h - 1700h	300.0	400	300.0	150.0	0	200.0	200.0	0	225.0
3	1800h - 2000h	300.0	400	300.0	200.0	207	150.0	300.0	80	150.0
4	2100h - 2300h	250.0	400	100.0	200.0	0	100.0	250.0	0	100.0

Table 1: Key driver variables for SAMI2 optimised against MIDAS, for different feature spaces and time windows during 20 November 2003.

4.1 Varying solar, geomagnetic and drift velocity variables

In the following investigations, the key driver variables varied for SAMI2 were $F_{10.7}$, Ap and V which are respectively a measure of solar radiation at 10.7cm wavelength, a measure of geomagnetic activity, and the maximum $\boldsymbol{E} \times \boldsymbol{B}$ drift velocity for the sinusoidal drift model (indirectly an indication of electric field strength). These driver variables were varied such that $F_{10.7} \in \{50.0, 100.0, 150.0, 200.0, 250.0, 300.0\}$, $Ap \in \{0, 15, 80, 207, 400\}$ which corresponds to $Kp \in \{0, 3, 6, 8, 9\}$, and $V \in \{100.0, 150.0, 200.0, 225.0, 300.0, 375.0, 450.0\}\text{ms}^{-1}$. All other driver variables were kept at fixed values unless otherwise stated.

Optimisation results are detailed in Table 1 for four different time windows and three different feature spaces. The results for the VTEC feature space suggest very high solar and geomagnetic activity, and very strong electric fields, were required to replicate the MIDAS reconstruction. Optimisation for mean ionospheric heights suggest lower activity and field strengths were required, in particular geomagnetic activity in all time windows except that between 1800h and 2000h UT. The third set of optimisations based on both VTECs and mean ionospheric heights is similar to that based on mean ionospheric heights alone, except for generally higher solar activities. The differences imply that there is complimentary information in VTECs and mean ionospheric heights and each feature space is by itself insufficiently descriptive (this is expected since VTEC is not necessarily perfectly correlated to mean ionospheric height). Alternatively the matching function may be too simple, especially in ignoring channel noise, or the set of drivers may be insufficiently descriptive. In practice, all three causes are likely. For the optimisation using VTEC features alone, Figure 5 plots the VTEC under the optimised drivers at selected times during the day. The plots show SAMI2 successfully modelled the build-up of plasma above the eastern coast and some of its corotation with the earth, though the plasma enhancement dissipated earlier in time than was suggested in the tomographic reconstruction.

Further insight can be gained by considering the sensitivity of the match to variations in the key driver variables, in particular the shape of each objective function f^s used in the optimisations. However rather than plot contour surfaces at equally spaced values for $f^s, s \in [1, 4]$, contours are plotted at 41 equally spaced values in the corresponding natural log domain,

$$g^s \quad = \quad \ln\Big\{f^s - \min_{\boldsymbol{u} \in U} f^s(\boldsymbol{u})\Big\}, \tag{8}$$

where U denotes the domain set of driver variables (here the domain set had 210 members)[1]. The resulting hypersurfaces, for the different feature spaces and time windows are plotted in Figures 3 and 4, where each row is for a different feature space and each column a different time window. The spectrum of colours from blue to red indicate increasing values for the relevant f^s value. However the smoothness of the contour surfaces may be misleading since the contours were obtained using a relatively small finite set of 210 domain points. The log operator accentuates functional differences near the functional minima.

There is little consensus in the shapes of the hypersurfaces for VTECs alone and mean ionospheric heights alone. This is consistent with there being complimentary information in the two feature spaces. However

[1]To avoid taking logs of zero, all function values for a particular $s \in [1, 4]$ were floored to a value between the most negative and second most negative value obtained in f^s; for integrity, contours were then plotted at and above the aforementioned second most negative value.

s	time window (UT)	description
1	1200h - 1400h	midrange to high V
2	1500h - 1700h	low to midrange V
3	1800h - 2000h	midrange to high V, high $F_{10.7}$
4	2100h - 2300h	low V, midrange to high $F_{10.7}$

Table 2: Location of minima for different time windows, based on general consensus between the VTEC and $\bar{h}$ feature spaces, for 20 November 2003.

the plots help reveal some limited agreement in the location of the minima, i.e. optimised driver values, as detailed in Table 2. The minima suggest high levels of solar activity were at times required by SAMI2 to heat up the ionosphere to produce enough plasma. Surprisingly, very high values of maximum drift velocity V were at times required; since this is an indirect indication of electric field strength, the analysis suggests very high field strengths were required to uplift plasma to altitudes where recombination rates were lower. The uplifted plasma should increase both the VTEC and mean ionospheric height calculated from the SAMI2 output. When viewed as a time series, the location of the minimum for VTECs moves fairly smoothly between time windows except for a large change between time windows 3 and 4. For $\bar{h}$ features, the minimum moves fairly smoothly except between time windows 1 and 2. Such discontinuities suggest rapid changes in the ionosphere triggered, perhaps after some delay, by rapid changes in the drivers.

Regarding sensitivity, the most notable characteristic of the plots is the relative insensitivity of the matching function to variations in geomagnetic activity for VTECs, as compared to $\bar{h}$ features. In general, the gradients in the matching function appear higher for the VTEC feature space than for the $\bar{h}$ feature space, implying VTECs may be generally more sensitive to variations in drivers than mean ionospheric heights. The structure in the hypersurfaces suggests there is some useful information which can be exploited for image-model coupling; however the relatively low resolution in the domain set U may mask significant 'noise' in the hypersurfaces, thereby degrading confidence in their usefulness for coupling.

4.2 Additionally varying the multiplicative factor for neutral O density

Next, an extra driver variable was introduced for the time window 1800h-2000h UT (this time window is near the peak of the storm according to the D_{st} index values detailed in Figure 6). The neutral O density was varied from its default using a multiplicative factor. This is expected to influence the ratio of densities of O^+ to N_2^+. Fast annealing with instant freezing was used to sample the values of the four driver variables, according to the algorithm in [18]. The sampling algorithm was initialised at $(F_{10.7}, Ap, V, k) = (300.0, 400, 300.0, 1.0)$ where k refers to the multiplicative factor for neutral O density and, here and below, V is in ms^{-1}. The drivers were sampled from the following domains; $F_{10.7} \in [100.0, 300.0], Ap \in [0, 400], V \in [100.0, 450.0], k \in [0.90, 5.00]$ where the quantisation was at 1, 0, 1 and 2 decimal places respectively. A total of 19 samples were drawn and tested using the schedule $(a_0, b) = (0.40, 0.2)$ to determine the rate of shrinkage of the sampling distribution; hence $a_0 = 0.40$ and $a_{19} = 0.01$ to 2 decimal places. This '19-sample process' was repeated 14 times, with the sampling algorithm reinitialised each time to the current best combination of drivers, i.e. the combination which gave the lowest value of the matching function. The sampling scheme did not therefore guarantee a global solution, only a better solution. The final solution was $(F_{10.7}, Ap, V, k) = (285.8, 396, 275.3, 1.26)$. The alternative solution due to the sampling process may be 'noisy', particularly when the solutions being sampled lie in a shallow basin of the matching function.

The optimised value $k = 1.26$ is a multiplying factor for the density of neutral O. Since the multiplicative factor for the neutral N_2 density was not varied but kept fixed at 1.0, the ratio of densities for neutral O to N_2 was increased by a factor of 1.26 (however it should be noted that the ratio of absolute densities was not directly specified). The results suggest that an increase in the ratio of neutral O to N_2 densities may well be responsible for some of the high electron content during the storm, as suggested in [3].

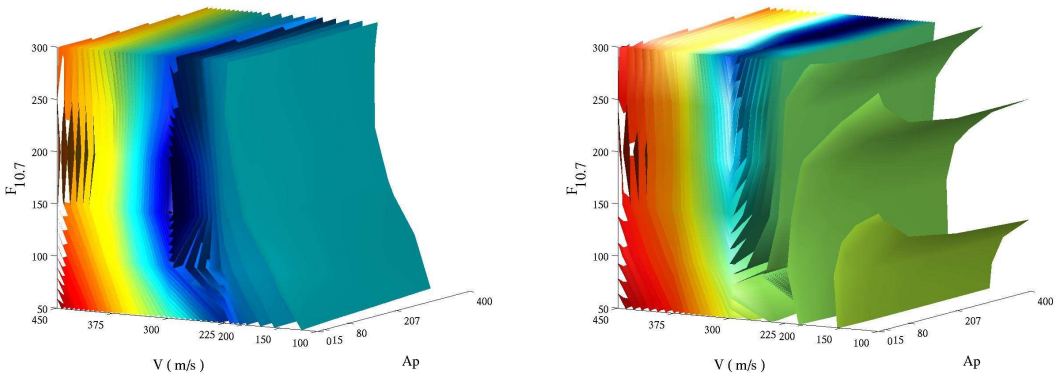

VTEC

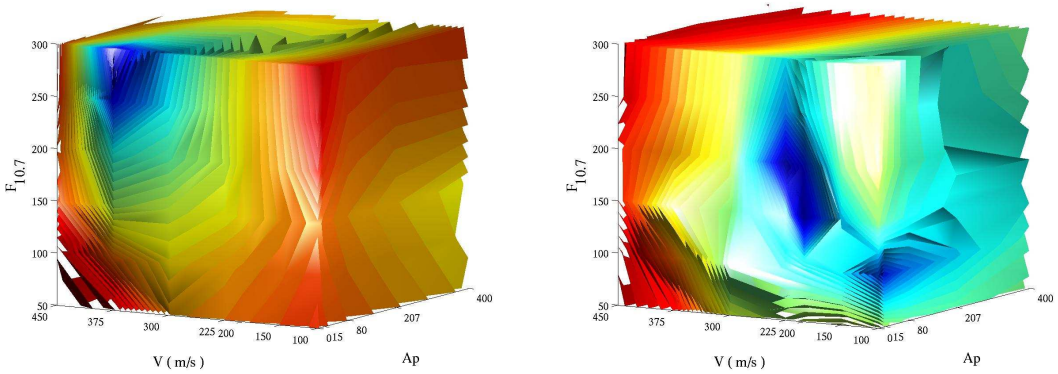

$\bar{h}$

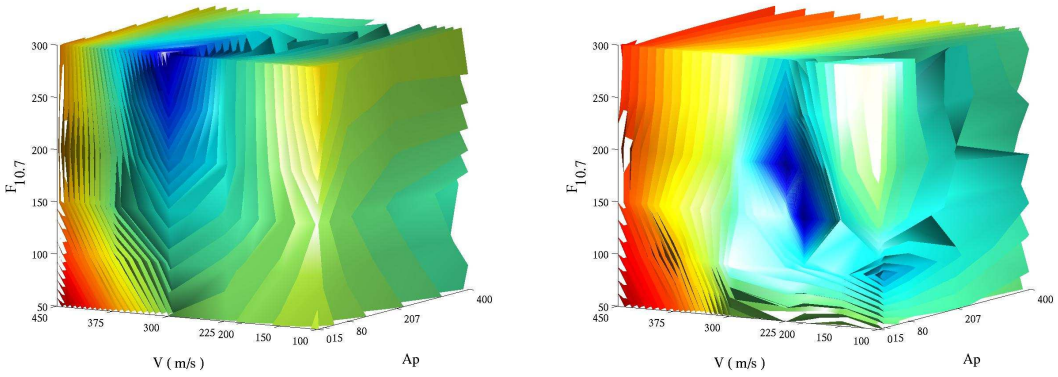

VTEC and $\bar{h}$

g^1 (1200h - 1400h UT) g^2 (1500h - 1700h UT)

Figure 3: Contour surfaces matching the SAMI2 output and MIDAS reconstruction for different feature spaces, and for different time windows during 20 November 2003.

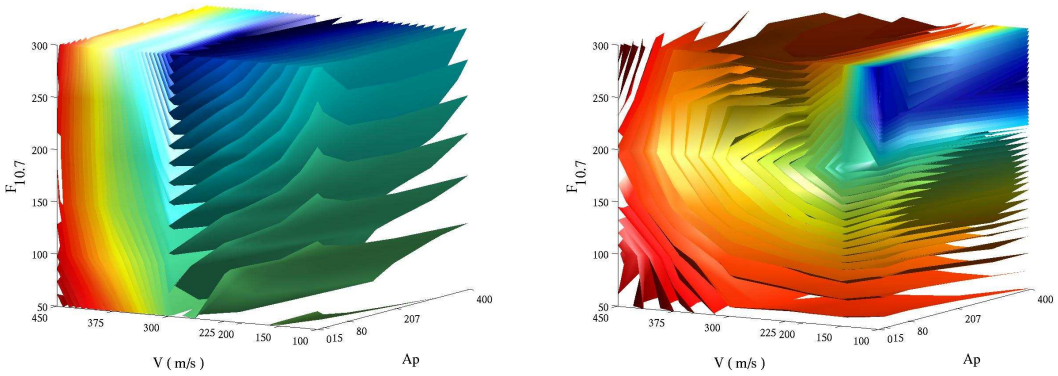

VTEC

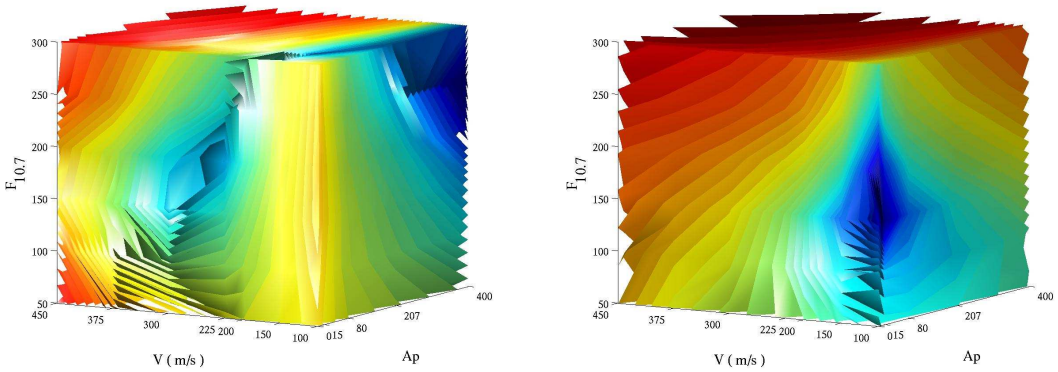

$\bar{h}$

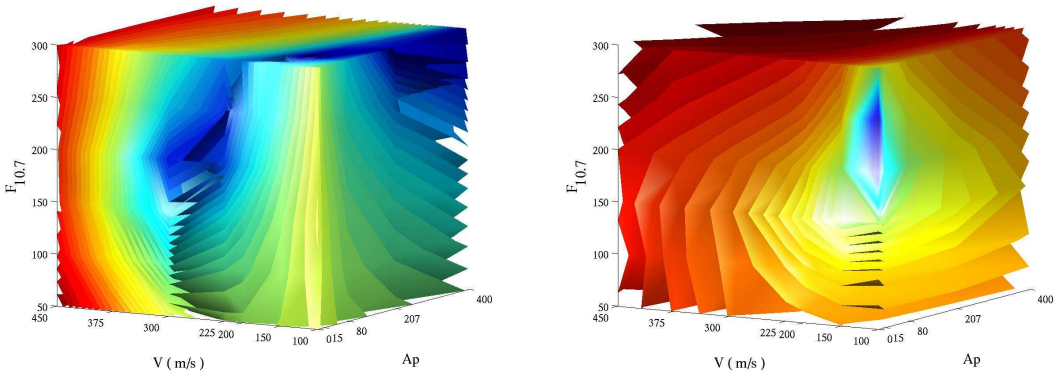

VTEC and $\bar{h}$

g^3 (1800h - 2000h UT) g^4 (2100h - 2300h UT)

Figure 4: Contour surfaces matching the SAMI2 output and MIDAS reconstruction for different feature spaces, and for different time windows during 20 November 2003.

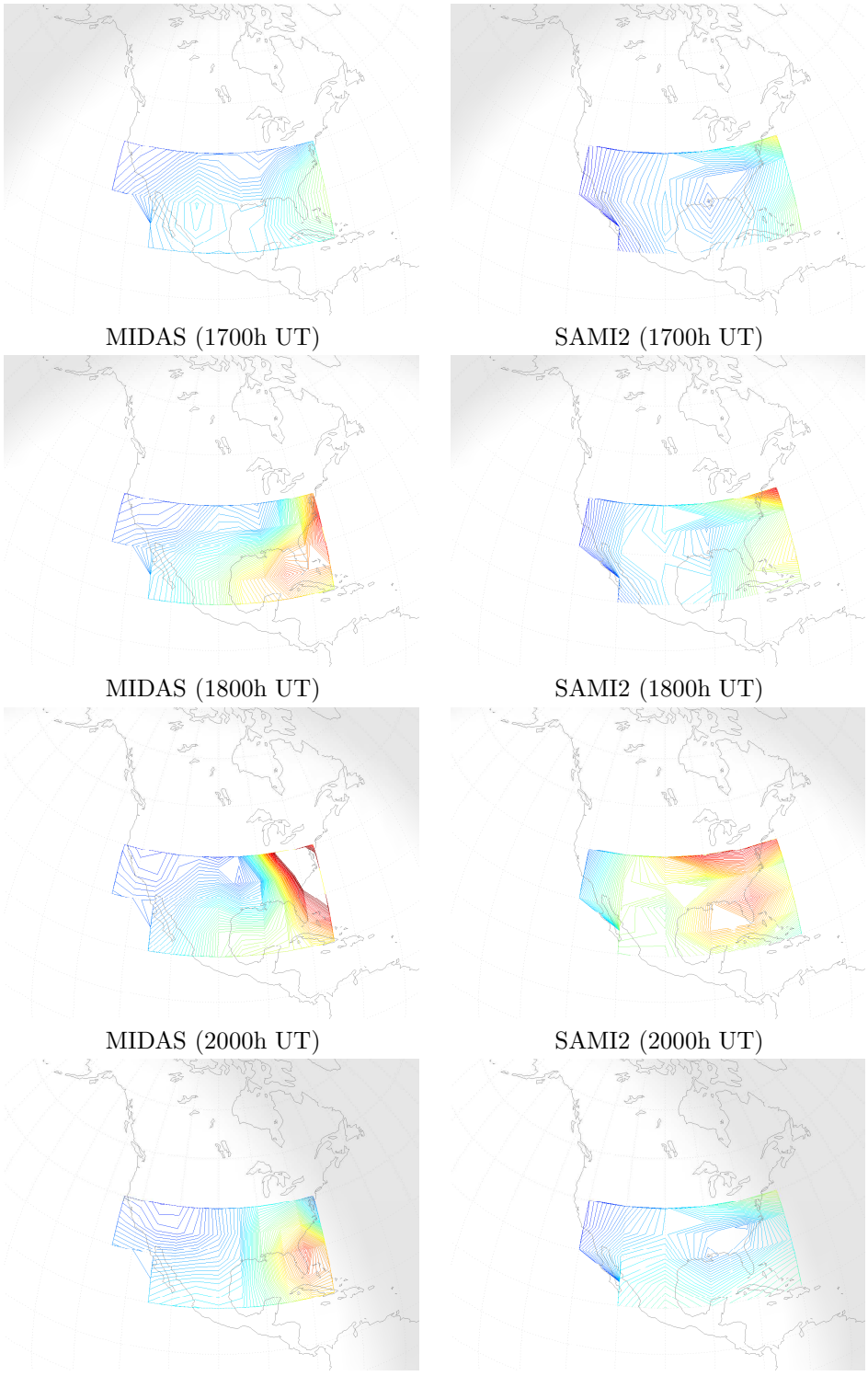

Figure 5: Contour plots of VTEC above the north America region for MIDAS and the optimised SAMI2 models for 20 November 2003 (0 to 100 TEC units in intervals of 1 TEC unit, where 1 TEC unit = $1{\times}10^{16}$ electrons/m^2).

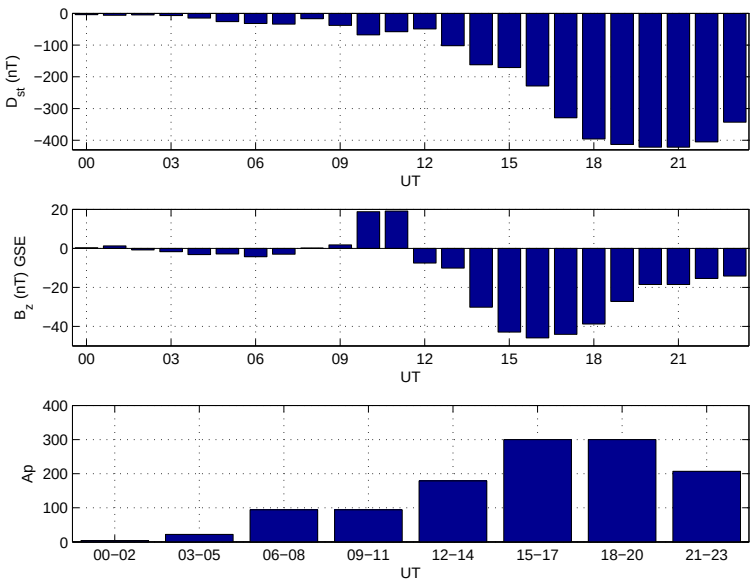

Figure 6: Hourly measurements for D_{st} and B_z, and three-hourly measurements for Ap (see [13] and the Acknowledgments).

Ideally the multiplicative factors for all ion species should be varied. However, a larger number of images must then be included in the matching process to avoid an 'overtrained' solution. Sensitivity analysis becomes more difficult as the size of the search space increases.

5 Discussion

Figure 6 details the variation of variables measured or calculated for the 20 November 2003. The D_{st} index shows that the storm peaks at 2000h/2100h UT, and the IMF B_z component that the storm, as expected, occurs during a southward orientation of the IMF (values for the IMF B_z component are also available at a higher sampling rate than hourly). In addition, the $F_{10.7}$ value for the day was 154 (this is the absolute solar radio flux as detailed on [20], see also the Acknowledgments). Perfect image-model coupling [18], providing it were possible, should recover the Ap and $F_{10.7}$ values exactly (however the coupling framework described in these experiments only has the ability to vary the $F_{10.7}$ value every 3 hours). There is discrepancy between the $F_{10.7}$ and Ap values recorded and those obtained by the optimisation for image-model coupling; in particular the optimised $F_{10.7}$ values appearing to be overestimates. This suggests that the coupling results, including the sensitivity analysis, should be interpreted cautiously. SAMI2 was designed to model equatorial and low latitude processes, rather than those high latitude processes which can have a significant effect at midlatitudes during a geomagnetic storm. For example, SAMI2 was not designed to accurately model the physics of high latitude convection, and the simple sinusoidal $\boldsymbol{E}\times\boldsymbol{B}$ drift velocity model is most applicable in equatorial regions. Furthermore, SAMI2 uses the HWM93 neutral wind model. This wind model is statistical and is unlikely to adequately or accurately characterise the strong high latitude equatorward neutral winds, caused by Joule heating and electron precipitation, common during a large storm. To illustrate this, a cursory investigation suggested an increase in the multiplicative factor for neutral winds actually decreased plasma in the L-shaped region, rather than increased the plasma as would be expected if high latitude winds were more accurately modelled. Similarly a decrease in the multiplicative factor actually yielded increased plasma rather than the expected decreased plasma. Since the L-shaped region chosen for the coupling experiments is at midlatitudes where both equatorial and polar/auroral processes are likely to be influential during a geomagnetic storm, SAMI2 may be replicating the build-up of plasma at high latitudes by driving an equatorial process in an unrealistic manner. In particular, the high $\boldsymbol{E}\times\boldsymbol{B}$ drift velocities near the equator

suggest the drift velocity model is too simple.

The SAMI2 sensitivity analysis confirmed that $F_{10.7}$, Ap, the $\boldsymbol{E} \times \boldsymbol{B}$ drift velocity parameter V, and the multiplicative factor for neutral O density all have an effect in replicating ionospheric electron content during this particular storm. Variation in the parameter V was used to mimic variation in electric field strength, while variation in the neutral O density was used to model variation in the ratio of neutral O to N_2 densities. In the sensitivity analysis for VTEC in [9], each driver variable was varied individually, but not in combination.

The image sequence was obtained by tomographic reconstruction and its accuracy is susceptible to sources of error. For example, there are false assumptions in the model underlying the tomographic technique, e.g. the linearisation, Gaussian and Markov assumptions inherent in the Kalman filter, the use of two empirical orthogonal functions to define vertical electron density profiles etc.. Furthermore, errors are likely where there is a geographically sparse or uneven distribution of IGS receivers [4] [15] (this motivated the choice of the L-shaped region used in the experiments, since north America is relatively rich in terms of the number of IGS receivers). It would be beneficial to repeat the analysis for a larger region. It may also be beneficial to compare model output and images at timesteps more frequent than one per hour. However high frequency comparison may necessitate the introduction of a matching function based on a channel model with more realistic assumptions of 'channel memory' [18].

More fundamentally, SAMI2 was used in the 'reverse direction' though it was designed to run in the 'forward direction', i.e. SAMI2 was used to discriminate the most appropriate drivers given electron content in the ionosphere, rather than 'generate' suitable electron content given drivers. For image-model coupling, it may be useful to introduce some techniques from discriminative learning [5] to help ionospheric models better discriminate different drivers given specific electron content.

SAMI2 models the distribution of plasma at different slices in geomagnetic longitude. There is no coupling between slices and no attempt to directly model zonal plasma drifts. Global models such as SAMI3 [17] may be more appropriate. The choice of a global model should balance accuracy with computational cost, particularly if the model has many input driver variables and any optimisation in the coupling process is likely to require many runs of the model. With high vertical $\boldsymbol{E} \times \boldsymbol{B}$ drift velocities, there is also the risk of introducing modelling innaccuracies if plasma is dragged down from the topmost field line to 1580km altitude (J.D. Huba, private communication).As an example, and as detailed in Appendix B, this is possible above the geomagnetic equator for $V \geq 95.4$ ms^{-1}, though the bound is more difficult to calculate elsewhere.

As explained in [18], those matching functions which account for 'channel memory' and more expressive 'source memory' may improve the coupling and sensitivity analysis. For example, some regularisation may be introduced which constrains the variation of key drivers between adjacent time windows. However an increase in the complexity of the matching function sometimes requires more data to estimate the accompanying statistical models robustly, or increased complexity in the search and optimisation. In general, more advanced optimisation techniques may be introduced. Particularly attractive are those derivative-free methods which numerically approximate the Hessian of the matching function as part of the optimisation process [14]. The Hessian may be regarded as encoding sensitivity information at a particular instantiation of driver variables, though relative to one image sequence only [18]. There may also be benefit in augmenting the feature space with new features. The analysis for SAMI2 above suggested that VTEC and mean ionospheric height contained complementary information. The careful selection and inclusion of extra features may give a fuller and better description of the ionosphere [18].

6 Conclusions

Image-model coupling can be used to infer the values of driver variables which best replicate some description of electron content in the ionosphere. Coupling may also be used to explore the sensitivity of the electron content to variations in the values of those driver variables. By way of illustration, an ionospheric

model has been coupled to a tomographic reconstruction of the geomagnetic storm of 20 November 2003. A relatively simple model was chosen and few input variables were varied. The investigation suggested there was merit in modelling an increase in the ratio of O to N_2 neutral densities during the storm. The conclusions drawn are limited by the validity of the assumptions in the ionospheric model and the accuracy of the tomographic images. In particular, better models of electric field strength during storm conditions would be advantageous. Image-model coupling may be used to give further insight into the physical processes at work in the ionosphere, and the limitations of the model being used.

A The $\boldsymbol{E} \times \boldsymbol{B}$ sinusoidal drift velocity model

The vertical component of the $\boldsymbol{E} \times \boldsymbol{B}$ drift velocity, according to the 'sinusoidal model' in [8], varies as the following scalar field. Expressing all angles in radians, unless otherwise stated, and defining a critical altitude h_{crit}, then the vertical component at altitude $h \geq h_{\text{crit}}$, geomagnetic latitude $\theta \in [-\pi/2, \pi/2]$ and local time t in hours is,

$$v(h, \theta, t) \quad = \quad V(h, \theta) \sin\big(\frac{\pi(t-7)}{12}\big), \tag{9}$$

where,

$$V(h, \theta) \quad = \quad V \quad \cos(\alpha(h, \theta)) \quad \frac{\cos^3(\theta)}{(1 + 3\sin^2(\theta))^{1/2}} \frac{(h+R)^2}{R^2}, \tag{10}$$

and where $\alpha(h, \theta)$ is the angle the magnetic field line at (h, θ) makes with the local horizontal, R is the radius of the Earth (in the same units as altitude), and V is the parameter quoted in the investigations. For $h < h_{\text{crit}}$, the term $V(h, \theta)$ decays exponentially. Hence V is simply a mathematical parameter which may be interpreted as the, usually hypothetical, peak $\boldsymbol{E} \times \boldsymbol{B}$ drift velocity at zero altitude at the geomagnetic equator, where such drift is strictly vertical. According to this model, the localised peak vertical drift velocity $V(h, \theta)$ increases quadratically with increasing altitude, but decreases northwards and southwards of the geomagnetic equator due to the convergence of field lines and their dipping relative to the local horizontal. As a result, the actual vertical $\boldsymbol{E} \times \boldsymbol{B}$ drift velocities at northerly latitudes are much less than those at the geomagnetic equator. For example, within the north America region used in the investigations between 90km and 1580km inclusive, approximate calculations gave the localised peak vertical drift velocity $V(h, \theta)$ as varying between $0.49V$ and $0.07V$ near 20°N and 40°N geographic latitude respectively, with an average of $0.20V$. For reference, between the same altitude limits and along the lines of geomagnetic longitude used in the experiments detailed above, the maximum vertical component of localised peak $\boldsymbol{E} \times \boldsymbol{B}$ drift velocity was approximated at $1.50V$ near the geomagnetic equator.

B Calculating plasma displacement due to $\boldsymbol{E} \times \boldsymbol{B}$ drift

At the geomagnetic equator plasma displacement is in the radial direction so that, applying the $\boldsymbol{E} \times \boldsymbol{B}$ drift velocity model described in Appendix A,

$$\frac{\mathrm{d}h}{\mathrm{d}t'} \quad = \quad V' \frac{(h+R)^2}{R^2} \sin(t'), \tag{11}$$

where $t' = \pi(t-7)/12$, t' is dimensionless and t is in hours, and where V' is expressed in units consistent with t' and altitude h such that the velocity V in ms^{-1} is,

$$V \quad = \quad \frac{1000 \times \pi}{12 \times 60^2} V'. \tag{12}$$

Between t'_1 and t'_2, assume it is physically possible to displace plasma from h_1 to h_2. Solving the ordinary differential equation [10],

$$\int_{h_1}^{h_2} \frac{R^2}{(h+R)^2 V'} \mathrm{d}h \quad = \quad \int_{t'_1}^{t'_2} \sin(t') \mathrm{d}t'. \tag{13}$$

Of interest is the velocity V' required to drag plasma down from h_1 to h_2 over half a day between $t'_1 = \pi$ and $t'_2 = 2\pi$,

$$V' = \frac{R^2}{2}\left(\frac{1}{(h_2+R)} - \frac{1}{(h_1+R)}\right). \quad (14)$$

Relating this to the investigations reported above, then when $h_1 = 10000$km, $h_2 = 1580$km and $R = 6365$km, then $V = 95.4$ ms^{-1}. This implies that when the parameter $V \geq 95.4$ ms^{-1}, plasma is dragged down in the $\boldsymbol{E} \times \boldsymbol{B}$ direction from the upper field line above the geomagnetic equator to the top of the grid structure at an altitude of 1580km. However it is more difficult to calculate the velocity parameter V which is required to potentially drag down plasma from above nonzero geomagnetic latitudes. Although the topmost field line has a lower altitude above such latitudes, the relevant peak $\boldsymbol{E} \times \boldsymbol{B}$ drift velocity there, according to the model, is also lower.

Acknowledgments

Approximately and in brief, N.D. Smith was responsible for conducting experiments, various parts of implementation, primary analysis of results, and writing; D. Pokhotelov gave invaluable help in analysis of results and ionospheric science; C.N. Mitchell gave the initial motivation, global experimental design, and helped in analysis of results; all helped in proofreading and giving suggestions. N.D. Smith and C.J. Budd were supported in BICS by EPSRC grant GR/S86525/01. For financial support, D. Pokhotelov would like to thank the STFC, and C.N. Mitchell the STFC and EPSRC. The authors would also like to thank Paul Spencer for his work in developing MIDAS including its visualisation software, the script which was modified only slightly for the MIDAS reconstruction, and for useful discussion; the Naval Research Laboratory for providing SAMI2, and J.D. Huba for helpful comments on SAMI2; the providers of IRI-95 [1]; the providers of OMNIWeb and the relevant data therein (see [13] for details); and the IGNSS services for providing the IGS data. The investigation used MATLAB.

References

[1] D. Bilitza. International Reference Ionosphere - Status 1995/96. *Advances in Space Research*, 20(9):1751–1754, 1997.

[2] G.S. Bust and C.N. Mitchell. History, current state, and future directions of ionospheric imaging. *Reviews of Geophysics*, 46, 2008. RG1003, doi:10.1029/2006RG000212.

[3] G. Crowley, C.L. Hackert, R.R. Meier, D.J. Strickland, L.J. Paxton, X. Pi, A. Mannucci, A.B. Christensen, D. Morrison, G.S. Bust, R.G. Roble, N. Curtis, and G. Wene. Global thermosphere-ionosphere response to onset of 20 November 2003 magnetic storm. *Journal of Geophysical Research*, 111, 2006. A10S18, doi:10.1029/2005JA011518.

[4] R.M. Dear and C.N. Mitchell. GPS interfrequency biases and total electron content errors in ionospheric imaging over Europe. *Radio Science*, 41, 2006. RS6007, doi:10.1029/2005RS003269.

[5] R.O. Duda, P.E. Hart, and D.G. Stork. *Pattern Classification*. A Wiley-Interscience Publication. John Wiley & Sons,Inc., Second edition, 2001.

[6] J.C. Foster, A.J. Coster, P.J. Erickson, W. Rideout, F.J. Rich, T.J. Immel, and B.R. Sandel. Redistribution of the Stormtime Ionosphere and the Formation of a Plasmaspheric Bulge. In J. Burch, M. Schulz, and H. Spence, editors, *Inner Magnetosphere Interactions: New Perspectives from Imaging*, volume 159 of *Geophysical Monograph Series*, pages 277–289. American Geophysical Union, 2005.

[7] J.K. Hargreaves. *The solar-terrestrial environment*. Cambridge atmospheric and space science series. Cambridge University Press, 2003.

[8] J.D. Huba, G. Joyce, and J.A. Fedder. Sami2 is Another Model of the Ionosphere (SAMI2): A new low-latitude ionosphere model. *Journal of Geophysical Research*, 105(A10):23035–23053, 2000.

[9] G. Jee, R.W. Schunk, and L. Scherliess. On the sensitivity of total electron content (TEC) to upper atmospheric/ionospheric parameters. *Journal of Atmospheric and Solar-Terrestrial Physics*, 67(11):1040–1052, 2005. doi: 10.1016/j.jastp.2005.04.001.

[10] G.A. Korn and T.M. Korn. *Mathematical Handbook for Scientists and Engineers: Definitions, Theorems, and Formulas for Reference and Review*. McGraw-Hill,Inc., second, enlarged and revised edition, 1968.

[11] A.J. Mannucci, B.T. Tsurutani, B. Iijima, A. Komjathy, B. Wilson, X. Pi, L. Sparks, G. Hajj, L. Mandrake, W.D. Gonzalez, J. Kozyra, K. Yumoto, M. Swisdak, J.D. Huba, and R. Skoug. Hemispheric Daytime Ionospheric Response To Intense Solar Wind Forcing. In J. Burch, M. Schulz, and H. Spence, editors, *Inner Magnetosphere Interactions: New Perspectives from Imaging*, volume 159 of *Geophysical Monograph Series*, pages 261–275. American Geophysical Union, 2005.

[12] C.N. Mitchell and P.S.J. Spencer. A three-dimensional time-dependent algorithm for ionospheric imaging using GPS. *Annals of Geophysics*, 46(4):687–696, 2003.

[13] OMNIWeb. Space Physics Data Facility, NASA/Goddard Space Flight Center, access: June 2008. http://omniweb.gsfc.nasa.gov.

[14] M.J.D. Powell. A view of algorithms for optimization without derivatives. *Mathematics TODAY*, 43(5):170–174, 2007.

[15] S.E. Pryse, L. Kersley, C.N. Mitchell, P.S.J. Spencer, and M.J. Williams. A comparison of reconstruction techniques used in ionospheric tomography. *Radio Science*, 33(6):1767–1779, 1998.

[16] SAMI2. The SAMI2 Open Source Project, Naval Research Laboratory, access: November 2007. http://wwwppd.nrl.navy.mil/sami2-OSP/index.html.

[17] SAMI3. NRL Ionosphere Model: SAMI3, access: September 2008. http://www.nrl.navy.mil/content.php?P=04REVIEW105.

[18] N.D. Smith, C.N. Mitchell, and C.J. Budd. Image-model coupling: a simple information theoretic perspective for image sequences, 2008. BICS preprint available at: http://www.bath.ac.uk/math-sci/bics/preprints/index.html.

[19] P.S.J. Spencer and C.N. Mitchell. Imaging of fast moving electron-density structures in the polar cap. *Annals of Geophysics*, 50(3):427–434, 2007.

[20] SPIDR. Space Physics Interactive Data Resource (SPIDR), National Geophysical Data Center (NGDC), NOAA Satellite and Information Service, access: June 2008. http://spidr.ngdc.noaa.gov.

[21] B.T. Tsurutani, O.P. Verkhoglyadova, A.J. Mannucci, T. Araki, A. Sato, T. Tsuda, and K. Yumoto. Oxygen ion uplift and satellite drag effects during the 30 October 2003 daytime superfountain event. *Annales Geophysicae*, 25:569–574, 2007. available at: http://www.ann-geophys.net/25/569/2007/.

[22] D.R. Weimer. Models of High-Latitude Electric Potentials Derived with a Least Error Fit of Spherical Harmonic Coefficients. *Journal of Geophysical Research*, 100(A10):19,595–19,607, 1995.